



Publication Year	2020
Acceptance in OA	2021-01-12T08:27:19Z
Title	Activity-rotation in the dM4 star Gl 729. A possible chromospheric cycle
Authors	Ibañez Bustos, R. V., Buccino, A. P., Messina, S., LANZA, Antonino Francesco, Mauas, P. J. D.
Publisher's version (DOI)	10.1051/0004-6361/202039164
Handle	http://hdl.handle.net/20.500.12386/29680
Journal	ASTRONOMY & ASTROPHYSICS
Volume	644

Activity–rotation in the dM4 star Gl 729

A possible chromospheric cycle[★]

R. V. Ibañez Bustos^{1,2}, A. P. Buccino^{1,3}, S. Messina⁴, A. F. Lanza⁴, and P. J. D. Mauas^{1,3}

¹ Instituto de Astronomía y Física del Espacio (CONICET-UBA), C.C. 67 Sucursal 28, C1428EHA-Buenos Aires, Argentina
e-mail: ribanez@iafe.uba.ar

² Departamento de Física, FI-Universidad de Buenos Aires, Buenos Aires, Argentina

³ Departamento de Física, FCEyN-Universidad de Buenos Aires, Buenos Aires, Argentina

⁴ INAF-Osservatorio Astrofisico di Catania, via S. Sofia 78, 95123, Catania, Italia

Received 11 August 2020 / Accepted 7 October 2020

ABSTRACT

Aims. Recently, new debates about the role of layers of strong shear have emerged in stellar dynamo theory. Further information on the long-term magnetic activity of fully convective stars could help determine whether their underlying dynamo could sustain activity cycles similar to the solar one.

Methods. We performed a thorough study of the short- and long-term magnetic activity of the young active dM4 star Gl 729. First, we analyzed long-cadence K2 photometry to characterize its transient events (e.g., flares) and global and surface differential rotation. Then, from the Mount Wilson *S*-indexes derived from CASLEO spectra and other public observations, we analyzed its long-term activity between 1998 and 2020 with four different time-domain techniques to detect cyclic patterns. Finally, we explored the chromospheric activity at different heights with simultaneous measurements of the $H\alpha$ and the Na I D indexes, and we analyzed their relations with the *S*-Index.

Results. We found that the cumulative flare frequency follows a power-law distribution with slope ~ -0.73 for the range 10^{32} – 10^{34} erg. We obtained $P_{\text{rot}} = (2.848 \pm 0.001)$ days, and we found no evidence of differential rotation. We also found that this young active star presents a long-term activity cycle with a length of about 4 yr; there is less significant evidence of a shorter cycle of 0.8 yr. The star also shows a broad activity minimum between 1998 and 2004. We found a correlation between the *S* index, on the one hand, and the $H\alpha$ the Na I D indexes, on the other hand, although the saturation level of these last two indexes is not observed in the Ca lines.

Conclusions. Because the maximum-entropy spot model does not reflect migration between active longitudes, this activity cycle cannot be explained by a solar-type dynamo. It is probably caused by an α^2 -dynamo.

Key words. stars: activity – stars: late-type – techniques: spectroscopic

1. Introduction

M dwarfs, with masses between 0.1 and 0.5 M_{\odot} , constitute about 75% of the stars in the solar neighborhood. Approximately half of them show high chromospheric activity that exceeds the activity of the Sun. They are usually referred to as dMe stars because they have $H\alpha$ in emission, or are called flare stars because they show frequent highly energetic flares (e.g., Günther et al. 2020; Rodríguez Martínez et al. 2020). The fraction of these active stars depends markedly on the spectral class (West et al. 2004, 2011; Reiners et al. 2012).

Stellar activity is assumed to be driven by a stellar dynamo. For solar activity in particular, this is the $\alpha\Omega$ dynamo, which is explained by the feedback between the differential rotation of the star, which stretches the lines of the poloidal magnetic field to produce a toroidal field (the Ω -effect), and the turbulent helical movements of the plasma in the convective zone, which regenerates the poloidal field (the α -effect, see Charbonneau (2010) for more details of the solar dynamo process). In several dynamo models (e.g., Charbonneau & MacGregor 1997;

Dikpati et al. 2005), the tachocline, an interface between the rigidly rotating radiative core and the convection zone, plays a fundamental role. A solar-type dynamo can also successfully reproduce stellar activity cycles in cooler stars (e.g., Buccino et al. 2020).

However, dM stars with masses lower than $\sim 0.35 M_{\odot}$ are thought to be fully convective (Chabrier & Baraffe 1997) and therefore should not have a tachocline. Despite this fundamental difference in stellar structure, strong magnetic activity is also observed in very low-mass fully convective stars (Mauas & Falchi 1996; Hawley et al. 1996; West et al. 2004). Furthermore, stellar activity cycles were also detected in these stars (Cincunegui et al. 2007a; Díaz et al. 2007b; Suárez Mascareño et al. 2016; Wargelin et al. 2017; Ibañez Bustos et al. 2019b). A new debate on the role of layers of strong shear has recently been initiated by Wright & Drake (2016). They suggested that the presence of a tachocline is not a critical ingredient in a solar-type dynamo. Based on this, Yadav et al. (2016) developed a dynamo model for the fully convective star Proxima Centauri and concluded that large Rossby numbers (the ratio of stellar rotation period to convective turnover time) may promote regular activity cycles in fully convective stars. Therefore observational evidence of cyclic activity near the convection threshold and beyond can contribute new insight into this discussion (Buccino et al. 2014; Ibañez Bustos et al. 2019b; Toledo-Padrón et al. 2019).

[★] Based on data obtained at Complejo Astronómico El Leoncito, operated under agreement between the Consejo Nacional de Investigaciones Científicas y Técnicas de la República Argentina and the National Universities of La Plata, Córdoba and San Juan.

The relation between stellar rotation and magnetic activity is another fundamental key to understanding the stellar dynamo. It shows an increase in activity when the rotation period decreases, with a saturated activity regime for fast rotators. This relation has been widely studied in different works using different indicators: by Wright et al. (2011, 2018), and Wright & Drake (2016) in X-ray emission (using L_X/L_{bol}), and by Astudillo-Defru et al. (2017) and Newton et al. (2017) in the optical range, employing the $\log(R'_{\text{HK}})$ and $L_{\text{H}\alpha}/L_{\text{bol}}$, respectively. In both the optical and X-ray ranges, these studies concluded that the transition in the inner structure of the stars does not imply a change in the dynamo mechanism (e.g., Wright & Drake 2016), and stellar rotation therefore plays an important role in driving the activity also in fully convective stars (e.g., Ibañez Bustos et al. 2019b). Even in this case, however, Astudillo-Defru et al. (2017) found three stars that do not belong to either of these regimes.

We study Gliese 729 in detail, which is one of the outliers in the saturation regime reported by Astudillo-Defru et al. (2017) because its $\log(R'_{\text{HK}})$ value deviates by more than 3σ from the fit (see Fig. 6 in Astudillo-Defru et al. 2017). We present a short- and long-term activity analysis of this star using high-precision photometry and a long series of spectroscopic observations. In Sect. 2, we describe some features that make Gl 729 a particularly interesting target. In Sect. 3, we provide an overview of our optical spectroscopic observations together with the archival data that we also employed for the analysis. In Sects. 4 and 5, we present a detailed analysis of the photometric and spectroscopic data with different time-domain techniques, and we explore the relation between different spectral features at different activity levels. Finally, in Sect. 6, we discuss the main conclusions of this analysis.

2. The target

Gl 729 (Ross 154, HIP 92403, V* V1216 Sgr) is an M4 active dwarf of the southern constellation of Sagittarius ($\alpha_{2000} = 18^{\text{h}}549^{\text{m}}49.4^{\text{s}}$, $\delta_{2000} = -23^{\circ}50'10''$). This single star is the seventh M dwarf closest to our Sun with a distance of 2.97 pc, a radius of $0.19 R_{\odot}$, and a mass of $0.14 M_{\odot}$ (Gaidos et al. 2014).

Gl 729 is a flare star that has been observed in the optical (Falchi et al. 1990; Astudillo-Defru et al. 2017), X-ray (Wargelin et al. 2008; Malo et al. 2014), and extreme-UV (EUV) ranges (Tsikoudi & Kellett 1997). First, Kiraga & Stepien (2007) reported a rotation period of $P_{\text{rot}} = 2.869$ d for Gl 729 using ASAS photometry, confirmed by Díez Alonso et al. (2019). Based on this period and its coronal activity level, given by $\log(L_X/L_{\text{bol}}) = -3.5$ (Johns-Krull & Valenti 1996), Gl 729 is below the saturation regime ($L_X/L_{\text{bol}} = 10^{-3}$) reported by Wright et al. (2011).

Wargelin et al. (2008) studied the coronal magnetic activity using two Chandra observations. One of them presents a very large flare with evidence of the Neupert effect. The other observation has several moderate flares. The authors found that the distribution of flare intensities does not appear to follow a single power law, as in the solar case. They analyzed the nonflaring phase to search for low-level flaring, and found that the microflaring explains the emission in this “quiescent” regime. They found that the normalized X-ray luminosity L_X/L_{bol} is below 10^{-3} , which is near the mean value of the saturation regime.

Because of their low masses, M dwarf stars are also ideal targets for detecting terrestrial planets from the ground (e.g., Anglada-Escudé et al. 2016; Ribas et al. 2018; Díaz et al. 2019) or from space (e.g., Muirhead et al. 2012; Winters et al. 2019).

Furthermore, statistical studies show a high occurrence of small planets around M stars (Bonfils et al. 2013; Dressing & Charbonneau 2015). However, activity features could hide an exoplanet signal and even mimic it (Robertson & Mahadevan 2014). Therefore, great efforts have been made to distinguish activity and planetary signals in the radial velocity series (e.g., Desort et al. 2007; Haywood et al. 2014; Díaz et al. 2016) or transiting curves (e.g., Boisse et al. 2012; Bonomo & Lanza 2012; Aigrain et al. 2016; Morris et al. 2020). For this reason, an exhaustive characterization of the stellar magnetic activity over different timescales might allow detecting extrasolar planets even around active stars. In particular, Gl 729 belongs to the CARMENES (Calar Alto high-Resolution search for M dwarfs with Exoearths with near-infrared and optical Échelle Spectrographs) input catalog (Reiners et al. 2018), which is not biased by the activity level. Although Gl 729 has been observed by different programs, it has not been studied in the optical range in detail. We present an extensive study of this dMe variable star based on almost 20 yr of spectroscopic observations.

3. Observations

The HK α Project was started in 1999 with the aim to study the long-term chromospheric activity of southern cool stars. In this program, we systematically observe late-type stars from dF5 to dM5.5 with the 2.15 m *Jorge Sahade* telescope at the CASLEO observatory, which is located at 2552 m above sea level in the Argentinian Andes. The medium-resolution echelle spectra ($R \approx 13,000$) were obtained with the REOSC¹ spectrograph. They cover a maximum wavelength range between 3860 and 6690 Å. We calibrate all our echelle spectra in flux using IRAF² routines and following the procedure described in Cincunegui & Mauas (2004). We here employed 19 observations distributed between 2005 and 2019. Each observation consists of two consecutive spectra with 45 min exposure time each, which are combined to eliminate cosmic rays and to reduce noise.

We complemented our data with public observations obtained with several spectrographs by the programs listed in Table A.1. Sixty echelle spectra were observed by HARPS, mounted at the 3.6 m telescope ($R \sim 115,000$) at La Silla Observatory (LSO, Chile), distributed over 2005 and the interval 2015–2017. Only one FEROS spectrum was available in our study. This spectrograph is placed on the 2.2 m telescope in LSO and has a resolution of $R \sim 48,000$. Four spectra were taken in 2011 and 2015 with UVES, attached to the Unit Telescope 2 (UT2) of the Very Large Telescope (VLT) ($R \sim 80,000$) at Paranal Observatory. Two medium-resolution spectra ($R \sim 8,900$) in the UVB wavelength range (300–559.5 nm) were obtained in 2014 with the X-shooter spectrograph, mounted at the UT2 Cassegrain focus also at the VLT. Finally, we employed 13 spectra from the HIRES spectrograph mounted at the Keck-I telescope that were observed in 1998 and 2010.

HARPS and FEROS spectra have been automatically processed by their respective pipelines^{3,4}, while UVES and X-shooter observations were manually calibrated with the

¹ <http://www.casleo.gov.ar/instrumental/js-reosc.php>

² The Image Reduction and Analysis Facility (IRAF) is distributed by the Association of Universities for Research in Astronomy (AURA), Inc., under contract to the National Science Foundation.

³ <http://www.eso.org/sci/facilities/lasilla/instruments/harps.html>

⁴ <http://www.eso.org/sci/facilities/lasilla/instruments/feros.html>

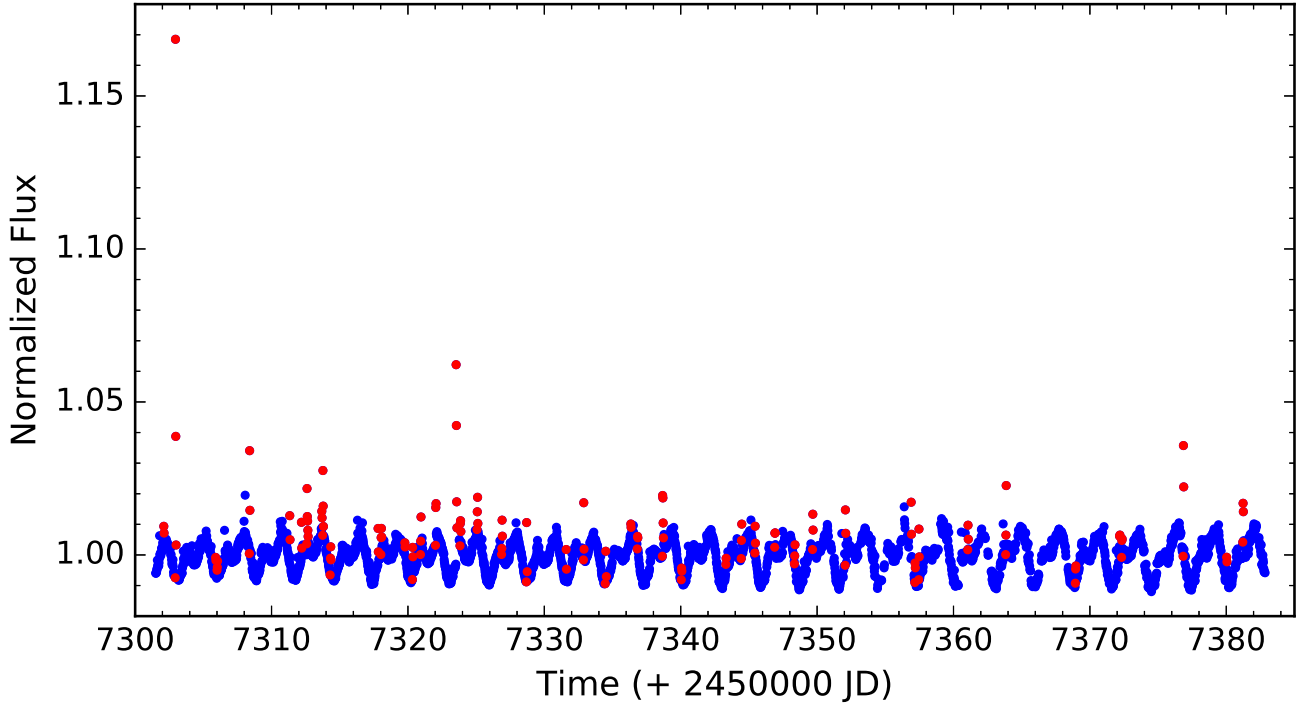


Fig. 1. Long-cadence K2 photometric light curve for Gl 729. Selected flare candidates are shown with red points.

corresponding procedure^{5,6}. We also analyzed high-precision photometry obtained during the K2 mission by the *Kepler* spacecraft (Borucki et al. 2010). K2 observed a total of 20 fields in sequential series of observational campaigns lasting ~ 80 d each. Throughout the mission, K2 observed in two cadence modes: short cadence (one observation every minute) and long cadence (one observation every ~ 30 min). In this study, we analyze the long-cadence observations of Gl 729 during campaign 7 of the GO7016_GO7060 proposal, obtained between 2015 October 4 and 2015 December 26.

4. Analysis of K2 photometry

In this section, we first present an analysis of the short-term activity of Gl 729, derived from the *Kepler* light curve. We also model the stellar variability with a maximum-entropy spot model to derive active longitudes and estimate a minimum amplitude for the stellar differential rotation.

4.1. Flare activity and rotation

To study the magnetic variability of Gl 729, we employed high-quality photometry obtained by the K2 mission. The *Kepler* database provides short- and long-cadence light curves, which constitute a great basis for detecting flare-like events (e.g., Hawley et al. 2014; Davenport et al. 2016). Only long-cadence photometry is available for Gl 729.

In order to analyze both the rotational modulation and detect these transient events in the *Kepler* light curve, we analyzed the time series with the flare detection with ransac method (FLATW’RM) algorithm based on machine-learning techniques

(Vida & Roettenbacher 2018)⁷. In particular, the FLATW’RM code first determines the stellar rotation period, and after subtracting the fitted rotational modulation from the light curve, it detects the flare-like events and reports the starting and ending time, and the time of maximum flare flux.

In Fig. 1, we show the photometric time series for Gl 729, where an appreciable rotational modulation can be noted. The red points indicate the flares detected by FLATW’RM for $N = 2$ and a detection limit of 3σ . These parameters were selected according to the statistical characteristics of flares of active M stars. According to Günther et al. (2020), the equivalent duration of a flare in an active M0–M4 or M4.5–M10 star lies between ~ 1 and ~ 120 min. Based on the 30-min cadence of the *Kepler* light curve in Fig. 1, we therefore requested at least two consecutive points above the detection limit to consider a single flare lasting at least 30 min. Shorter flares could not be detected with this sampling. We found a total of 47 flare events in ~ 81 days. The flare energy can be estimated by integrating the flare-normalized intensity during the event between the beginning and the end times detected by the algorithm (see Vida & Roettenbacher 2018 for more details). This equivalent duration ε_f is multiplied by the quiescent stellar luminosity (F_\star), to obtain the energy in the observed passband (ξ_f). We estimated the quiescent luminosity by integrating a flux calibrated X-shooter spectrum of Gl 729, convolved with the *Kepler* response function, to obtain the observed quiescent luminosity in the *Kepler* pass band, and we obtain $F_\star = 1.3 \times 10^{30}$ erg s⁻¹.

Following the analysis of Gizis et al. (2017), we studied the cumulative flare frequency distribution ν (i.e., the number of flares with a given energy or greater divided by the total time of observation in the light curve). It can be expressed as

$$\log \nu = a + \beta \log \xi_f. \quad (1)$$

⁵ <http://www.eso.org/sci/facilities/paranal/instruments/uves.html>

⁶ <http://www.eso.org/sci/facilities/paranal/instruments/xshooter.html>

⁷ FLATW’RM is available at <https://github.com/vidakris/flatwrm/>

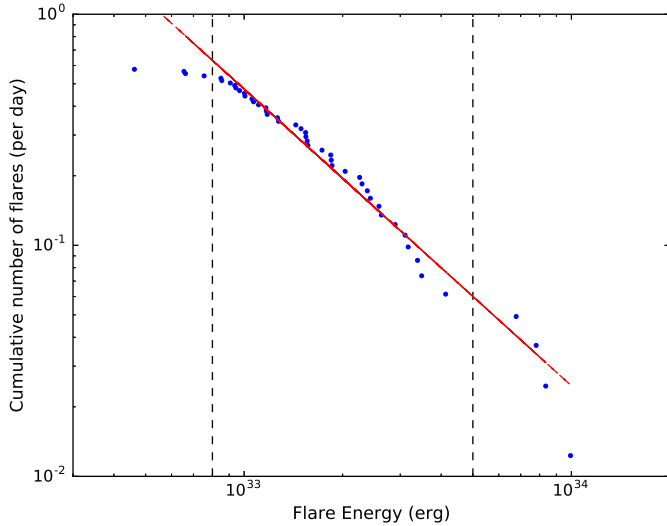


Fig. 2. G1 729. Cumulative frequency of flares ν derived from the *Kepler* light curve with the FLATW’RM algorithm. The red solid line is the best linear fit (Eq. 1) in the range 8×10^{32} – 5×10^{33} erg with $\alpha = 1.71$.

The slope $\beta = (1 - \alpha)$ is found by fitting the distribution by a linear function, where α is used to characterize how the flare energy of the star is dissipated. In Fig. 2, we show the best linear fit for the energy range indicated with dashed black lines. We obtained a value of $\alpha = 1.71$ from this least minimum-squares fit. Gizis et al. (2017) proposed an alternative method for calculating α using a maximum likelihood estimator for the small sample size,

$$(\alpha - 1) = (n - 2) \left[\sum_{i=1}^n \ln \frac{\xi_i}{\xi_{\min}} \right]^{-1}, \quad (2)$$

where n is the number of transient events and ξ_i and ξ_{\min} are the individual and lowest flare energies, respectively. With this method, we obtain $\alpha = 1.73$, which is consistent with the linear-fit value.

Thus, G1 729 flares follow a power-law slope $\beta \sim 0.71$ between 10^{32} and 10^{34} erg. Considering that the energy flux in the quiescent state is around 10^{30} erg s $^{-1}$, the energy release during a flare event is larger by 2–4 orders of magnitude than the time-integrated stellar luminosity.

To analyze the rotational modulation, we discarded the flares detected by FLATW’RM. We studied the resulting light curve, shown in Fig. 3, using the generalized Lomb–Scargle (GLS) periodogram (Zechmeister & Kürster 2009) in Fig. 4. The most significant period we detected is the rotation period found in the literature (see Sect. 2). We obtained $P_{\text{rot}} = (2.848 \pm 0.001)$ days with a high significance (false-alarm probability, FAP < 0.1%). We also found a second peak of $P = (1.427 \pm 0.001)$ days, half P_{rot} , with lower significance. Following Lamm et al. (2004), we estimate the error of the detected period as $\delta P = \frac{\delta \nu P^2}{2}$, where $\delta \nu$ is the finite frequency resolution of the periodogram. In Fig. 3, we also plot the best fit with two harmonic functions of these two periods with a red line.

This bimodality could be associated to two dominant spots in opposite hemispheres, with areas A_1 and $A_2 < A_1$. This case would be equivalent to having a symmetric spot with area A_2 in both hemispheres that rotate with $P_{\text{rot}}/2$ and an asymmetric spot with area $A_1 - A_2$ in only one hemisphere that rotates with P_{rot} . McQuillan et al. (2013) performed a statistical analysis of *Kepler*

light curves of a series of M stars and found that several stars of their sample present this bimodality in their rotation periods.

4.2. Spot modeling

A critical ingredient of the $\alpha\Omega$ dynamo is the differential rotation in the stellar interior (e.g., convection zone). A good proxy might be its surface differential rotation (see, e.g., Buccino et al. 2020), which can be derived from the stellar spot migration.

When the light curve is phased with the average rotation period, the mean longitude of the activity centers at latitudes with rotation either shorter or longer than the average period are expected to migrate. Spot modeling is one possible approach to infer such a migration.

We applied a spot modeling approach that was introduced in Bonomo & Lanza (2012), to which we refer for details. In brief, the surface of the star is subdivided into 200 surface elements that contain unperturbed photosphere, dark spots, and solar-like faculae. The specific intensity of the unperturbed photosphere in the *Kepler* passband is assumed to vary according to a quadratic limb-darkening law,

$$I(\mu) = I_0(a_p + b_p\mu + c_p\mu^2), \quad (3)$$

where I_0 is the specific intensity at the center of the disk, $\mu = \cos \theta$, with θ being the angle between the local surface normal and the line of sight, and a_p , b_p , and c_p are the limb-darkening coefficients in the *Kepler* passband (Claret & Bloemen 2011).

The dark spots are assumed to have a fixed contrast $c_s \equiv I_{\text{spot}}(\mu)/I(\mu)$ in the *Kepler* passband, where I_{spot} is the specific intensity in the spotted photosphere. The fraction of a surface element covered by dark spots is given by its filling factor f .

This model is fit to a segment of the light curve of duration Δt_f (see Sect. 4.3) by varying the filling factors of the individual surface elements that can be represented as a 200-element vector \mathbf{f} . The spot pattern is assumed to stay fixed in each interval of duration Δt_f , which is a fundamental assumption of our modeling because a significant spot evolution that would occur on a shorter timescale may hamper our approach.

Our model has 200 free parameters and is nonunique and unstable because of the effect of photometric noise. To select a unique and stable solution, we applied a maximum entropy regularization by minimizing a functional Z that is a linear combination of the χ^2 and of a suitable entropy function E ,

$$Z = \chi^2(\mathbf{f}) - \lambda E(\mathbf{f}), \quad (4)$$

where $\lambda > 0$ is a Lagrangian multiplier that controls the relative weights given to the χ^2 minimization and the configuration entropy of the surface map E in the solution. The expression of E is given in Eq. (4) of Lanza et al. (1998) and it is maximum when the star is unspotted, that is, all the elements of the vector \mathbf{f} are zero. In other words, the maximum entropy (hereafter ME) criterion selects the solution with the minimum spotted area compatible with a given χ^2 value of the best fit to the light curve. When the Lagrangian multiplier $\lambda = 0$, we obtain the solution corresponding to the minimum χ^2 that is unstable. By increasing λ , we obtain a unique and stable solution at the price of increasing the value of the χ^2 . An additional effect is that the residuals between the model and the light curve become biased toward negative values because we reduce the spot filling factors by introducing the entropy term (see Lanza 2016, for more details).

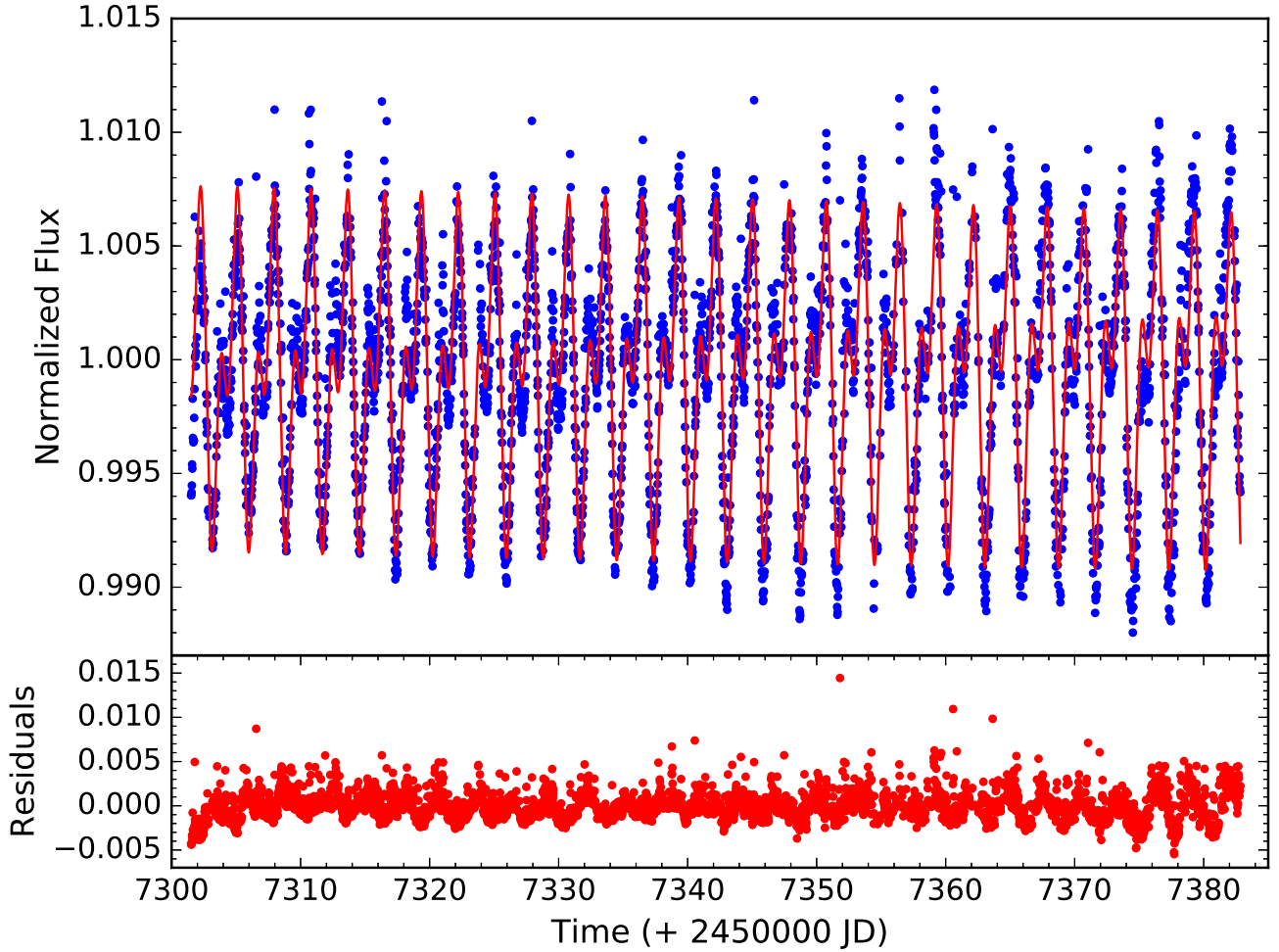


Fig. 3. K2 long-cadence photometry for Gl 729 without the flare candidates detected with the FLATW²RM algorithm. The solid red line represents the least-squares fit with two harmonic function of the periods found with the GLS periodogram (2.848 days and 1.427 days).

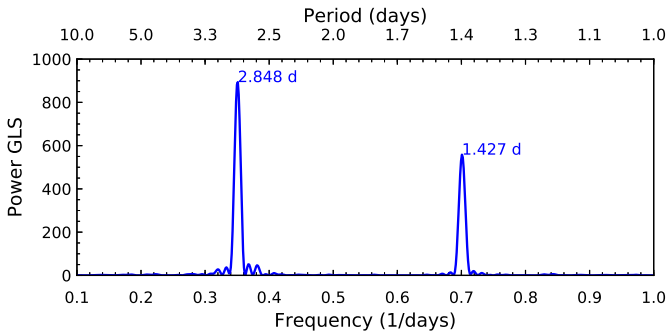


Fig. 4. GLS periodogram for the nonflaring K2 light curve of Fig. 3.

The information on the latitude of the spots is lacking in our ME maps because the inclination of the stellar spin axis is very close to 90° (cf. Sect. 4.3), which makes the transit time of each feature independent of its latitude. We therefore limit ourselves to map the distribution of the filling factor versus longitude.

The optimal value of the Lagrangian multiplier λ is obtained by imposing that the mean μ_{reg} of the residuals between the regularized model and the light curve verify the relationship (Bonomo & Lanza 2012; Lanza 2016)

$$|\mu_{\text{reg}}| = \frac{\sigma_0}{\sqrt{N}}, \quad (5)$$

where σ_0 is the standard deviation of the residuals of the unregularized model, that is, the model computed with $\lambda = 0$, and N the number of data points in the fitted light curve interval of duration Δt_f .

The optimal value of Δt_f is not known a priori and must be determined with an analysis of the light curve itself because it is related to the lifetimes of the active regions in a given star. We adopted a unique value of Δt_f for the entire light curve of Gl 729 because the ratio $\Delta t_f / P_{\text{rot}}$, where P_{rot} is the stellar rotation period, rules the sensitivity of the spot modeling to active regions located at different longitudes, as discussed by Lanza et al. (2007).

The optimal value of the facular-to-spotted area ratio Q could also be derived from the light curve best fit. Considering that at the young age of Gl 729 the activity is dominated by dark spots, and considering that for any value of Q , we found highly structured maps that barely represent the double-dip shape of the light curve. We therefore decided to fix $Q = 0$, that is, we included only dark spots in our model.

4.3. Stellar parameters

The basic stellar parameters, that is, mass, radius, and effective temperature T_{eff} , were taken from the references in Table 1. They do not directly enter our geometric spot model, except for the computation of the relative difference ϵ_{rot} between the polar

Table 1. Parameters adopted to model the light curves of Gl 729.

Parameter	Value	Ref.
Star mass (M_{\odot})	0.14	Gaidos et al. (2014)
Star radius (R_{\odot})	0.19	Gaidos et al. (2014)
T_{eff} (K)	3213	Gaidos et al. (2014)
$v \sin i$ (km s^{-1})	3.5 ± 0.5	Johns-Krull & Valenti (1996)
a_p	0.2023	Claret & Bloemen (2011)
b_p	1.1507	Claret & Bloemen (2011)
c_p	-0.3530	Claret & Bloemen (2011)
P_{rot} (days)	2.848	Present study
ϵ_{rot}	4.1×10^{-5}	Present study
i (deg)	90.0	Present study
c_s	0.90	Andersen & Korhonen (2015)
Q	0.0	Present study
Δt_f (days)	2.848	Present study

and equatorial axes of the ellipsoid used to represent the surface of the star. Their values are obtained by a simple Roche model assuming rigid rotation with a period of $P_{\text{rot}} = 2.848$ days. The gravity-darkening effect associated with $\epsilon_{\text{rot}} \sim 4.1 \times 10^{-5}$ is much smaller than the photometric precision, thus it can be neglected in our model. The inclination of the stellar rotation axis was assumed to be $i = 90^\circ$ because a star viewed equator-on is compatible with the stellar radius, the rotation period, and the projected rotational velocity $v \sin i$.

The contrast of the dark spots $c_s = 0.90$ was inferred from the work of Andersen & Korhonen (2015). The duration of the individual segments of the light curves was kept at $\Delta t_f = 2.848$ days, that is, the rotation period. We found that increasing Δt_f decreases the total χ^2 . In contrast, keeping $\Delta t_f = 2.848$ days, we obtain a better time resolution in the description of the spot evolution because the timescale of the active region growth and decay in Gl 729 is comparable to or longer than the rotation period. Choosing Δt_f equal to the rotation period is also optimal because it grants a uniform sampling of all the longitudes by our spot modeling (Lanza et al. 2007).

To infer information on the age, we checked possible membership with known associations or moving groups using the BANYAN Σ tool (Gagné et al. 2018). We found a 99.9% probability that Gl 729 is a field star. Using relations between age, rotation period, and X-ray luminosity ($\log L_X = 27.05$; Wright et al. 2011) calibrated for M2-M6 stars (Engle & Guinan 2018, 2011), we infer an age in the range from 0.2 to 0.6 Gyr. This result is supported by the relatively high rotation velocity ($v \sin i = 3.5 \pm 0.5 \text{ km s}^{-1}$) reported by Johns-Krull & Valenti (1996), which indicates that Gl 729 is a young star with an estimated age younger than 1 Gyr.

4.4. Model results

As mentioned in Sect. 4.2, we found the standard deviation σ_0 of the residuals of the unregularized model (obtained by imposing $\lambda = 0$) to be $\sim 1.1 \times 10^{-3}$ and the average number of data points in the fitted light curve interval of duration Δt_f to be $N \simeq 110$. After a number of trials, we found Eq. (4) to be satisfied with $|\mu_{\text{reg}}| \sim 1.0 \times 10^{-4}$. In Fig. 5, we show an example of the results of our spot modeling for the epochs from BJD 2 457 340.26 until 2 457 343.11, spanning a single stellar rotation.

In the top panel, we show the normalized flux with the best fit overplotted, in the middle panel, the distribution of residuals,

and finally, in the bottom panel, the spot maps at five selected rotation phases. Two major spot groups of different sizes in opposite hemispheres are clearly visible, which is compatible with the discussion in Sect. 4.1. We note that the *Kepler* K2 PDCSAP fluxes used in our analysis show evidence of residual instrumental effects, which are more clearly visible in the residual plot as discontinuities about every 0.1 intervals in rotation phase. However, the computed model (solid line) is apparently not affected by this issue.

As anticipated, we are specifically interested in verifying the possible migration of the longitude at which spots are located. This is accomplished in Fig. 6, where we plot the distribution of the filling factor of the starspots f versus the longitude and the time for the regularized spot maps. The origin of the longitude is at the meridian pointing toward the Earth on BJD 2 457 303.243, and the longitude increases in the same direction as the stellar rotation. We identify two activity centers, a dominant one located at about longitude zero, and another smaller center in the opposite hemisphere. These centers could be associated to the two peaks observed in the GLS periodogram of Fig. 3, one corresponding to the rotation period and the other to its first harmonic. We note some indication of an oscillation in the longitude of the dominant activity center. However, the amplitude of this migration, which is about 50° , is comparable to or smaller than the longitude resolution achieved by our spot modeling.

Our spot modeling allows us to determine the variation in total spotted area versus time by integrating the filling factor over the longitude. The error is estimated from the photometric accuracy of the data points. The gaps inside each individually fit interval of duration Δt_f affects the total area because the maximum entropy regularization drives the solution toward the minimum spotted area compatible with the data, thus reducing the filling factor at the longitudes that are in view during the gaps in the light curves.

To reduce this effect on the variation of the entire spotted area, we measured the presence of significant gaps in each interval Δt_f . We divided each interval into five equal subintervals and counted the number of data points in each subinterval n_i , with $i = 1, \dots, 5$ numbering the subinterval. A measure δ of the inhomogeneous distribution of the data points in the interval Δt_f is defined as $\delta \equiv [\max(n_i) - \min(n_i)] / \max(n_i)$. The intervals with $\delta > 0.2$ are discarded, giving a total of 21 area measurements that are not affected by the gaps in a total of 27 intervals.

The plot of the total spotted area versus the time for this light curve is shown in Fig. 7. The duration of the time interval is too short to conclude about the cause of the area variation, which might be associated with the growth and decay of the individual active regions in the active longitudes.

5. Chromospheric activity

In this section, we analyze the long-term activity of the flare active M4 dwarf, Gl 729. We present a magnetic activity analysis by compiling our own and public spectroscopic data and building a registry of activity that allows us to detect cyclic patterns.

5.1. Mount Wilson S-index

Stellar activity cycles have been detected in several late-type stars, typically by measuring fluctuations in the well-known dimensionless Mount Wilson S-index (e.g., Baliunas et al. 1995; Metcalfe et al. 2013; Ibañez Bustos et al. 2019a). This activity indicator S is defined as the ratio between the chromospheric

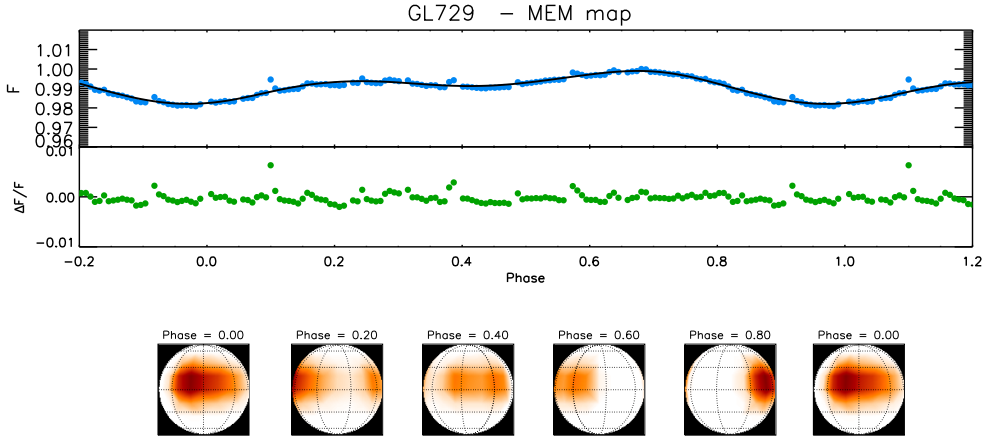


Fig. 5. Example of spot modeling of a single stellar rotation.

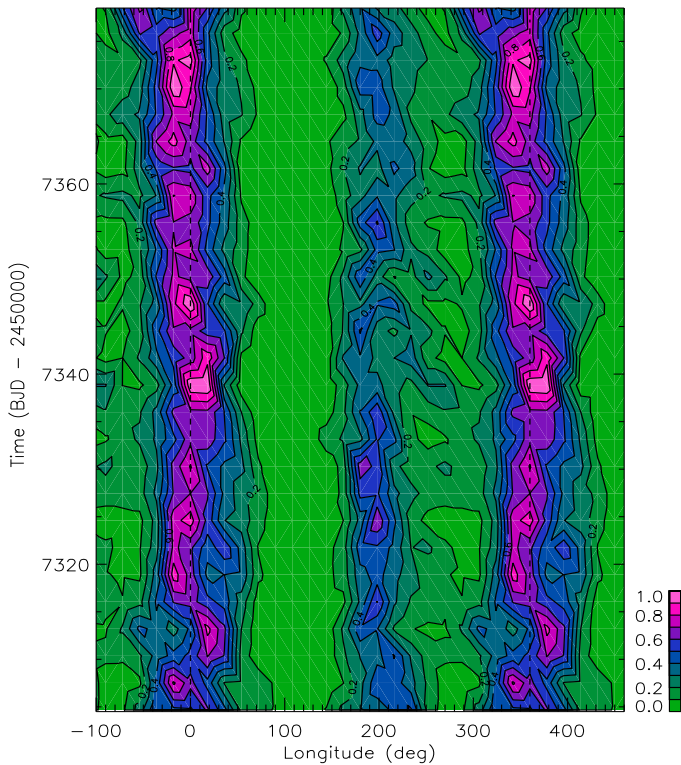


Fig. 6. Distribution of the spot filling factor versus longitude and time as derived by our maximum-entropy spot model. The maximum of the filling factor is indicated in purple and the minimum in green (see the color scale in the lower right corner). We note that the longitude scale is repeated beyond the $[0^\circ, 360^\circ]$ interval.

Ca II H and K line-core emissions, integrated with a triangular profile of 1.09 \AA full width at half maximum (FWHM), and the photospheric continuum fluxes integrated in two 20 \AA passband centered at 3891 \AA and 4001 \AA (Duncan et al. 1991). For decades, the S -index was mainly used to study the chromospheric activity only for dF to dK stars (Baliunas et al. 1995) because longer exposure times are needed to observe the Ca II lines in later stars, which are both redder and fainter. Cincunegui et al. (2007b) studied the usefulness of the S index and other activity indicators for dM stars.

To search for indications of stellar activity in Gl 729, we computed the S -index for the spectra mentioned in Sect. 3. For our CASLEO observations, we used the method described in

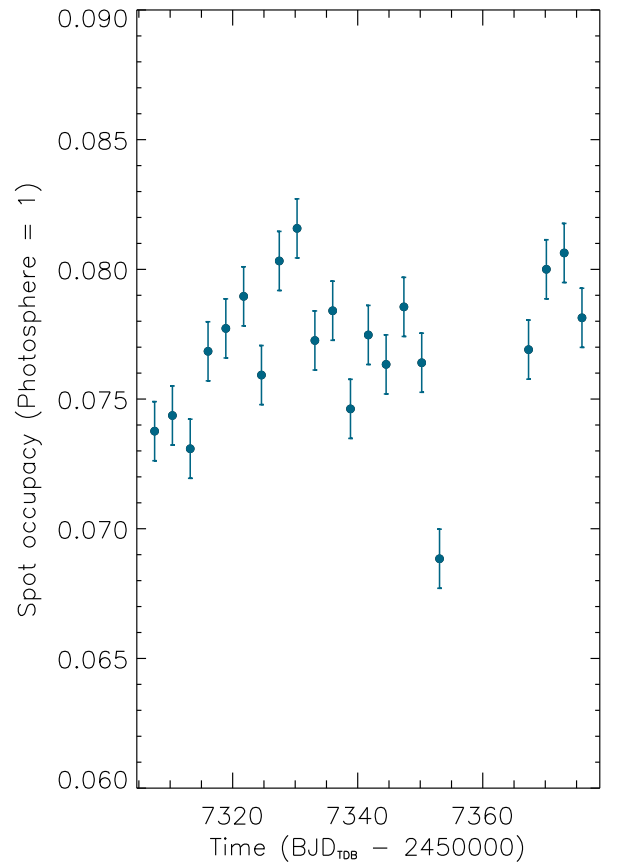


Fig. 7. Total spotted area as derived from the ME best fits to the light curve versus time. The error bars have an amplitude of 3σ , where σ is the standard deviation as derived from the photometric accuracy of the data points.

Cincunegui et al. (2007b). For the other spectra, we followed Duncan et al. (1991). We then calibrated the HARPS indexes to the Mount Wilson S -index with the calibration available in Lovis et al. (2011), and the FEROS spectra with the procedure used in Jenkins et al. (2008). Finally, as we have done in previous work (Ibañez Bustos et al. 2019a,b), we intercalibrated the CASLEO, FEROS, UVES, X-shooter, and HIRES indexes considering as reference the calibrated HARPS Mount Wilson indexes closest in time. Our time series is composed of 99 measurements for a time span between 1998 and 2019. These data are shown in Fig. 8 and listed in Table A.1.

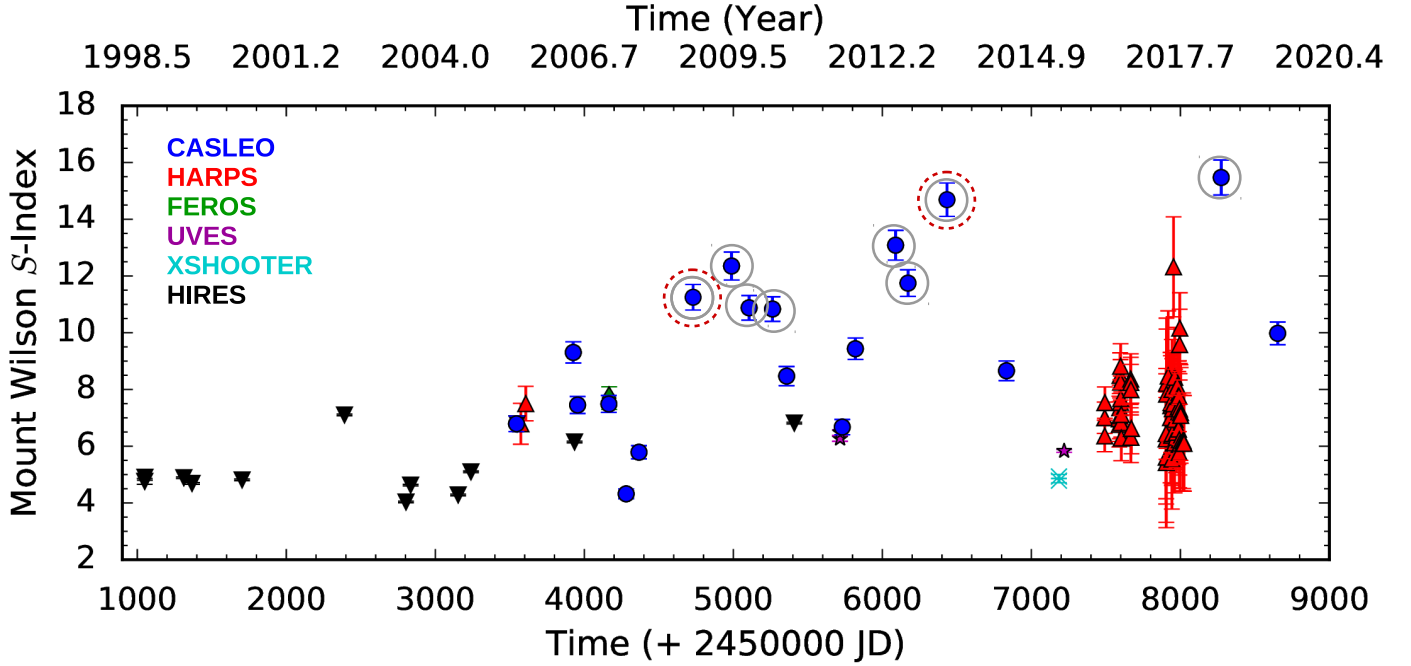


Fig. 8. Mount Wilson S -indexes for Gl 729 derived from CASLEO (blue circles), HARPS (red triangles), FEROS (green diamonds), UVES (magenta stars), X-shooter (cyan cross), and HIRES (black inverted triangles) spectra. We highlight the CASLEO spectra where an increase in activity is observed with gray circles. We show the two observations we discarded from our analysis as dashed red circles.

We estimated a 4% typical error of the S -index derived from CASLEO (see the deduction in [Ibañez Bustos et al. 2019a](#)). The error bars of the S -indexes derived from HARPS, FEROS, UVES, X-shooter, and HIRES spectra were calculated as the standard deviation of each monthly bin. The rotational modulation in the S -index may contribute to its daily variation; we estimated it to be $\sim 15\%$ from HARPS observations. For time intervals with only one ESO observation in a month, we adopted the typical RMS dispersion of the bins. The whole time series presents a variability of $\sigma_S/\langle S \rangle \sim 27\%$ in 21 yr.

5.2. Long-term variations

The time series plotted in Fig. 8 shows an almost flat regime between 1998 and 2004, and then an increasing trend until the maximum in 2018 ($xJD = 8300$ days). First, we analyzed if this growth is due to the gradual increase of the mean magnetic activity or to particular observations of transient high-energy phenomena (e.g., flares). Gl 729 has a flare frequency of 0.5 flares per day of at least 10^{33} erg (see Fig. 2). To filter these events out, we visually compared the individual spectra that form each of our observations (see Sect. 3) for the dates marked with gray circles in Fig. 8.

In Fig. 9, we show the individual line profiles of the Ca II K line for these observations. We show in red the first and in green the second observation. There is a difference of 85% between the two spectra taken in September 2008 (0908), and a difference of 78% between those taken in May 2013 (0513). We excluded these two observations from our analysis because they were probably obtained during flares. For the observation taken in June 2018 (0618) we see a difference of almost 38% between individual spectra. In this case we decided to include only the first observation (red line in Fig. 9) because its line flux is similar to that of the remaining nonflaring observations. The difference between the two fluxes in the other observations ranges from

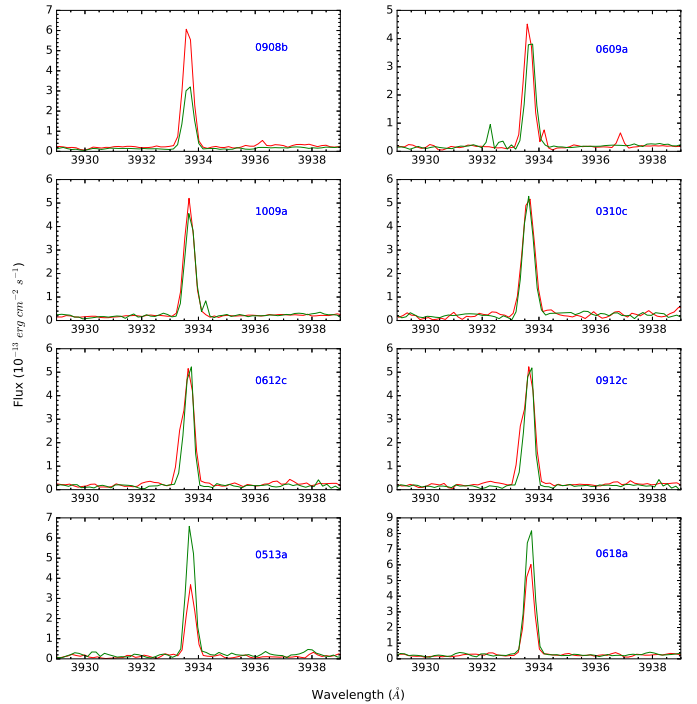


Fig. 9. Ca II K line for individual CASLEO observations. Each plot is labeled with the date of each observation (MMYY). We plot the first observation in red and the second consecutive observation in the same night in green.

6% to 11%, consistent with the calibration error ([Cincunegui & Mauas 2004](#)).

From the remaining data, we obtained a mean Mount Wilson index $\langle S \rangle = 7.343 \pm 1.967$ and a Ca II emission level of

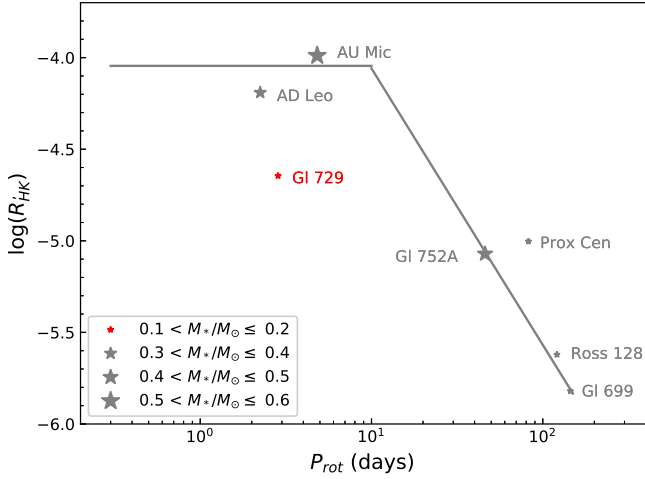


Fig. 10. $\log R'_{\text{HK}} - P_{\text{rot}}$ diagram including the fit of Astudillo-Defru et al. (2017) (gray solid lines). We show five M dwarfs whose activity cycles were detected using CASLEO spectra with gray stars (Prox Cen: Cincunegui et al. (2007a); GI 752A: Buccino et al. (2011); AD Leo: Buccino et al. (2014); AU Mic: Ibañez Bustos et al. (2019a), and Ross 128: Ibañez Bustos et al. (2019b)). The activity cycle of GI 699 was detected by Toledo-Adrón et al. (2019) employing seven independent sets of spectroscopic observations. We represent GI 729 with a red star. It is a clear outlier from the saturated regime of this diagram.

$\log R'_{\text{HK}} = -4.645$, which both agree with the values reported by Astudillo-Defru et al. (2017). Considering the rotation period for GI 729 of 2.848 days, the $\log R'_{\text{HK}}$ confirms that this star is an outlier in the saturation regime reported for dM stars in the $\log R'_{\text{HK}} - P_{\text{rot}}$ diagram (Astudillo-Defru et al. 2017). In Fig. 10, we plot the fit obtained by Astudillo-Defru et al. (2017) from the HARPS database. We also include five stars for which magnetic activity cycles were detected employing CASLEO spectra and GI 699 (Barnard’s star), whose activity cycle was reported by Toledo-Adrón et al. (2019) using a different set of spectroscopic data.

To search for long-term activity cycles in the remaining data series, we implemented three different methods. In the top panel of Fig. 11 we show the GLS periodogram together with the results of the CLEAN deconvolution algorithm developed by Roberts et al. (1987). Both analyses show a very significant peak at $P_1 = (1521 \pm 20)$ days for the GLS, a slightly higher value for the CLEAN periodogram, and a less significant one at $P_2 = (297 \pm 2)$ days, both with an FAP < 0.1%.

In Fig. 11 (bottom), we present the results of the Bayesian generalized Lomb-Scargle periodogram described by Mortier et al. (2015), which expresses “the probability that a signal with a specific period is present in the data”. The green line indicates the logarithmic probability, and the dashed magenta line shows the linear probability. We therefore conclude that both cycles are present in the data, although the about 1500-day activity cycle, with a 99% probability, is markedly more significant than the cycle with $P = 296$ days.

Böhm-Vitense (2007) examined the relation between P_{rot} and P_{cyc} for a set of cyclic FGK stars, expanding the work done previously (Brandenburg et al. 1998; Saar & Brandenburg 1999). She found that most stars are well distributed in two branches in the $P_{\text{cyc}} - P_{\text{rot}}$ diagram (her Fig. 2). A possible interpretation is that each sequence corresponds to a different type of dynamo. When we include our results in this $P_{\text{cyc}} - P_{\text{rot}}$ diagram, we find that the 1500-day cycle belongs to the active branch labeled “Aa” in that figure. For the stars in this branch, the number

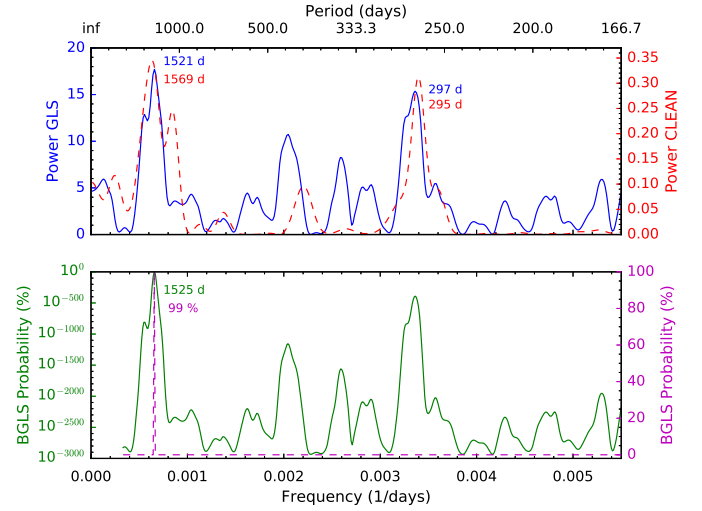


Fig. 11. Top: GLS (solid blue line) and CLEAN (dashed red line) periodograms for the S time series of GI 729. The most prominent peaks for the GLS periodogram with an FAP < 0.1% are (1521 ± 20) days and (297 ± 2) days. Bottom: Bayesian percentage probability indicates the 99% probability that the approximately 1500-day peak is the real activity cycle.

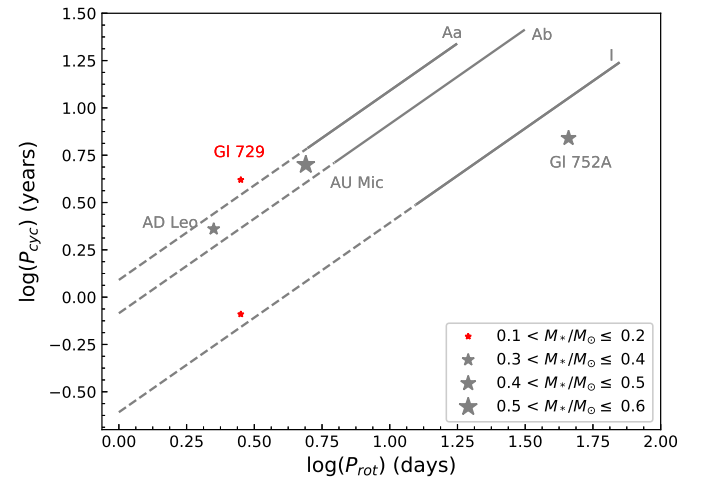


Fig. 12. $\log P_{\text{cyc}}$ versus $\log P_{\text{rot}}$. The solid gray lines represent the active (Aa and Ab) and inactive (I) branches reported in Böhm-Vitense (2007). We indicate the extrapolation to lower rotation periods with dashed lines. Gray stars represent the activity cycle periods obtained for the early-M dwarfs GI 752A (Buccino et al. 2011), AD Leo (Buccino et al. 2014), and AU Mic (Ibañez Bustos et al. 2019a). The red stars represent the periods of GI 729 we report here.

of rotational revolutions per activity cycle is about $P_{\text{cyc}}/P_{\text{rot}} \sim 500$, which is consistent with the value of $1521/2.848 = 534$ we obtain for GI 729. Similarly, the less significant activity cycle of $P_{\text{cyc}} \sim 300$ days lies within the inactive branch, where the ratio $P_{\text{cyc}}/P_{\text{rot}} \sim 90$. Furthermore, as we have shown in Sect. 4.3, GI 729 is a young star, which is coherent with the conclusion by Böhm-Vitense (2007) that stars that belong to the Aa sequence are younger than the Sun. This suggests that Böhm-Vitense’s diagram can be extended to cyclic M stars. In Fig. 12, we show the updated version of Fig. 2 from Böhm-Vitense (2007), and we include one dM and three dMe stars for which we found magnetic activity cycles.

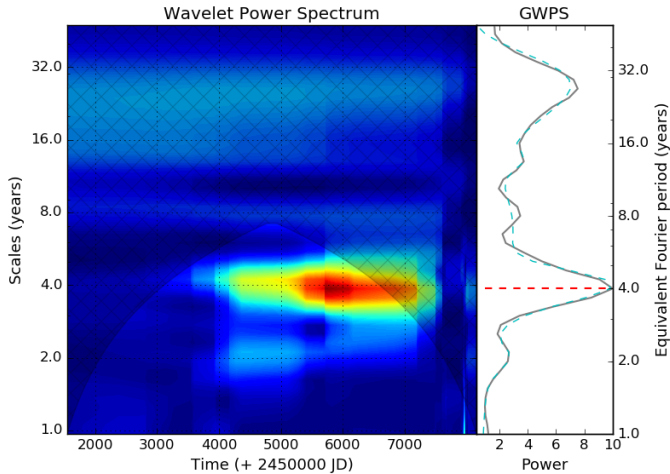


Fig. 13. Contour wavelet plot for Gl 729, calculated using the S time series of Fig. 8. The GWPS is plotted to the right and is fit by a sum of Gaussians (dashed cyan line). The horizontal dashed red line in the GWPS represents the maximum peak.

5.3. Wavelet analysis

To explore the strength of the periodic signals we found over time, we performed a wavelet analysis of the seasonal mean S -index measurements by implementing the wavelet analysis described in Torrence & Compo (1998) with the correction developed in Liu et al. (2007). It consists of repeatedly convolving a selected waveform, commonly called the mother wavelet, with the data at each time step, using a range of scales for the waveform. Each scale is associated with a different frequency. The power obtained in each convolution produces a frequency map against the time domain.

We used the Morlet wavelet, which is a sinusoidal signal with a Gaussian amplitude modulation. By sliding it along the time series and changing the scale of the wavelet (i.e., its frequency or period), we obtained the wavelet power spectrum (WPS) as the result of the correlation between the wavelet and the data.

Figure 13 shows the WPS for the time series of Fig. 8. The region delimited by the cross-hatched area is the wavelet region in which the edge effects become important, generally defined as the cone of influence. Inside the cone, the power spectrum is shown with a color scale going from the weakest (dark blue) to the strongest (red and brown) signals. We note a significant periodic signal between 3 and 5 yr.

We also obtained the global wavelet power spectrum (GWPS), defined as the sum of the WPS over time for each period of the wavelet. We show the GWPS at the right side of Fig. 13. Following García et al. (2014), we fit the GWPS with a sum of Gaussian curves associated with each peak. The extracted global period corresponds to the highest amplitude peak, and its uncertainty is the half-width at half maximum (HWHM) of the corresponding Gaussian profile. The horizontal dashed red line in the GWPS represents the most significant peak $P_{\text{wave}} = 4.1 \pm 0.7$ yr (1497 ± 256 days), in agreement with the 1521-day period detected with the periodograms above.

Additionally, the wavelet analysis allows us to study the distribution of the cyclic signal throughout the time series. Figure 13 shows that the 4-yr period maintains its strength for most of the observations. However, before xJD ~ 4000 days, the magnetic activity remains almost constant and the periodic signal is nearly insignificant (see Fig. 13). At about xJD = 4000 days, the activity level of Gl 729 increases and the cyclic activity

becomes more evident, until it reaches a peak after xJD ~ 6000 , observed in red in the WPS map in Fig. 13. Therefore we see here the same behavior as in Fig. 8.

This phase of flat activity in the range xJD = 1000–4000 days in Gl 729 resembles the well-known solar Maunder or Dalton Minima, although the sampling in this interval is rather poor and we are probably missing short term variations. Similarly, other solar-type stars also present this behavior: a broad activity minimum has also been observed in the K2V star ε Eridani (Metcalf et al. 2013) and in the G2V star HD 140538 (Radick et al. 2018). However, this is the first time that it is reported for an M star. Another possible interpretation is that a decadal activity cycle modulates the 4-yr cycle, although further observations of Gl 729 are required to confirm this hypothesis.

5.4. Sodium and $H\alpha$ as activity indicators

The Ca II lines are not the most adequate feature to study chromospheric activity in M stars, which are too faint in this region of the spectrum. To overcome this problem, it is necessary to explore redder activity indicators in these stars. For instance, the $H\alpha$ line has been extensively used as an activity indicator (Giampapa & Liebert 1986; Cincunegui et al. 2007b; Robertson et al. 2014), as were other lines, for example, the Na I D lines (Díaz et al. 2007a; Gomes da Silva et al. 2012).

The analysis of different chromospheric lines does not only allow us to study magnetic activity at different heights of the atmosphere, but also to understand the energy transport in these regions for different activity levels in M stars. In particular, atmospheric models of M stars show that the Ca II K line is formed in the lower chromosphere, while the $H\alpha$ line is formed in the upper chromosphere with a different formation regime (e.g., Mauas & Falchi 1994, 1996; Mauas et al. 1997; Fontenla et al. 2016). Walkowicz & Hawley (2009) observed a strong positive correlation between single observations of the Ca II lines and $H\alpha$ in most M3 V active stars. However, this relation is not always valid for multiple observations of an individual active star (Buccino et al. 2014).

The spectra we use in this paper, with the exception of those taken by HIRES and FEROS, cover a wavelength range that allows us to explore different chromospheric features. In particular, we inspect the correlation of simultaneous measurements of the Ca II lines with the $H\alpha$ and Na I D lines obtained for 94 and 87 spectra, respectively. To do so, we computed the sodium Na index and the $H\alpha$ index as defined by Gomes da Silva et al. (2012) and Cincunegui et al. (2007b), respectively. The results are shown in Fig. 14, and in the fifth column of Table A.1 we indicate the spectra used in this analysis as “y/y”.

The separation into two groups is clear in both cases. We separated the points with strong magnetic activity marked with gray circles in Fig. 8, which are indicated with magenta squares. For the remaining points, marked in blue, we found strong correlations in both cases, with Pearson coefficients $R = 0.86$ for $H\alpha$ and $R = 0.79$ for Na, as reported by Walkowicz & Hawley (2009) and Díaz et al. (2007a). The variability ($\sigma_X/\langle X \rangle$) of the $H\alpha$ and Na indexes during the cycle (blue points) is about 11 and 12%, respectively, much smaller than the S -index variability, which is about 27%.

This strong positive correlation seems to change in the activity cycle phase. The $H\alpha$ index seems to saturate at a value ~ 2.3 at the maximum of the activity cycle (gray points in Fig. 8). Furthermore, it is remarkable that this saturation level is lower than the maximum value reached by the $H\alpha$ index. A similar behavior, but with much more spread, is observed in the Na index.

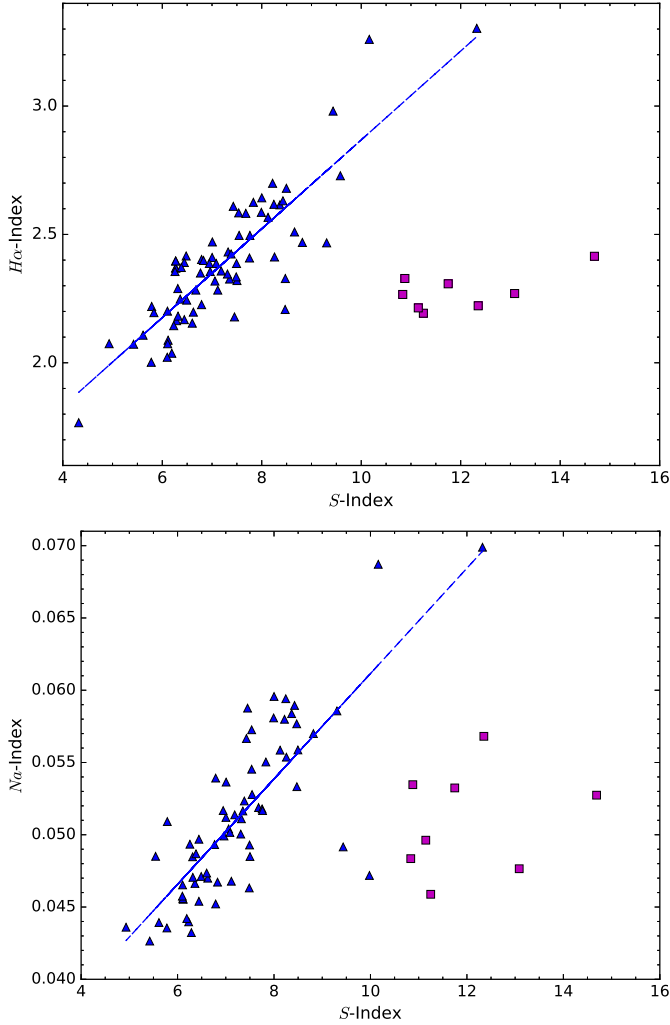


Fig. 14. Simultaneous measurements of the $H\alpha$ (*top*) and the Na I (*bottom*) indexes versus the Mount Wilson S -index for spectra that include the two features. The magenta squares indicate the points at which the magnetic activity level increased, some of them associated with flares (gray circles in Fig. 8).

This saturation might be due to a geometric effect: higher line-fluxes with activity can be due to a larger filling factor of active regions. The area covered by these active regions increases with height as the magnetic flux tubes spread out, however. While the filling factor increases, these tubes approach each other, until they eventually cover the entire surface higher up in the chromosphere, at the height where $H\alpha$ and the Na D lines are formed, reaching saturation.

6. Conclusions and summary

New interests in the magnetic activity of M stars have emerged in the past decades. On the one hand, their strong and moderate flares might severely constrain the habitability of a terrestrial planet (e.g., Buccino et al. 2007; Vida et al. 2017). On the other hand, due to their internal structures, almost and fully convective stars might be special laboratories for testing the dynamo theory. Nevertheless, magnetic activity cycles seem to be present in early, mid-, and late-M dwarfs (e.g., Cincunegui et al. 2007a; Buccino et al. 2011, 2014; Wargelin et al. 2017; Ibañez Bustos

et al. 2019a,b; Toledo-Adrón et al. 2019). Furthermore, regardless of whether these stars are fully convective, they are placed indistinctly in the two regimes that are usually observed in the relation of magnetic activity with the stellar parameters (e.g., L_X/L_{bol} versus P_{rot}/τ in Wright et al. 2011, 2018; $\log R'_{\text{HK}}$ versus P_{rot} in Astudillo-Defru et al. 2017). Thus, the change in the internal structure does not affect the activity–rotation relationship. One of our main conclusion is that stellar rotation could drive the activity in partly and fully convective stars.

We have contributed to this discussion with an exhaustive study of the fast rotator dM4 active star, Gl 729. First, we studied its short-term variability due to flares and rotation by a detailed analysis of the long-cadence *Kepler* light curve. We found that this active star presents a flare frequency of 0.5 flares per day with energies between 10^{32} and 10^{34} erg, which implies that energy release during these transient events reaches two or four orders of magnitude more than the quiescent level. Similar flares were also observed in other M stars (e.g., Hawley et al. 2014; Günther et al. 2020). After discarding the observations associated with flares in the *Kepler* light curve, we obtained a double-peaked harmonic curve associated with a rotation period of 2.848 days.

Long-term activity of M stars has been scarcely explored in comparison to solar-type stars. In this work, we derived the Mount Wilson S index using CASLEO, HARPS, FEROS, UVES, X-shooter, and HIRES spectra. For the whole time series covering 21 yr (1998–2019), we detected two significant periods of ~ 4.2 yr and ~ 0.8 yr with four different tools. Based on our wavelet analysis in Fig. 13, we can determine the distribution of the cyclic signal. We suspect that the 4.2-yr period is modulated by a decadal activity cycle presenting a minimum in the time range $x\text{JD} = 1000\text{--}4000$ days. Although this behavior has been observed in several solar-type stars (Metcalf et al. 2013; Radick et al. 2018), it has never been reported in M dwarfs.

We also derived a mean activity level of $\log R'_{\text{HK}} = -4.645$ in the time span, in agreement with the value reported in Astudillo-Defru et al. (2017). Nevertheless, given its rotation period, Gl 729 is placed markedly below the saturation regime in the $\log R'_{\text{HK}}$ versus P_{rot} diagram (see Fig. 10), probably indicating that its activity could be driven by a type of dynamo different than for other stars in the graph.

In order to explore the nature of the mechanisms responsible for the cyclical long-term activity detected in Gl 729, we analyzed its surface differential rotation, which is a necessary ingredient for the $\alpha\Omega$ dynamo operation (Charbonneau 2010), whereas it seems not to be determinant in turbulent α^2 dynamos (e.g., Durney et al. 1993; Chabrier & Küker 2006). To do so, we studied the *Kepler* light curve with the spot model described in Sect. 4.2. In this analysis, we identified two active longitudes, and we note some indication of an oscillation in the longitude of the dominant center of activity. However, the amplitude of this migration, which is about 50° , is comparable with the longitude resolution achieved by our spot modeling and it is therefore no evidence of surface differential rotation. Thus, the activity cycle of Gl 729 could be driven by a turbulent α^2 dynamo.

Cole et al. (2016) studied the oscillatory α^2 dynamo for a 1D mean-field dynamo model. They concluded that long activity cycles can be driven by an α^2 dynamo under certain conditions if the turbulent diffusivity profile is fairly concentrated toward the equator.

Furthermore, the two activity cycles detected in Gl 729, within the statistical error, belong to the active and inactive branch in the $P_{\text{cyc}} - P_{\text{rot}}$ diagram in Böhm-Vitense (2007). Although this diagram is mainly composed of FGK stars whose

activity cycles are probably well reproduced by a solar-type dynamo (e.g., Buccino et al. 2020), this bimodal distribution in $P_{\text{cyc}} - P_{\text{rot}}$ could be extended to all cyclic stars, independently of the underlying type of dynamo (see Fig. 12). All these facts make Gl 729 an ideal target for an exploration with dynamo models because it shows signs of long-term cyclic magnetic activity, without evidence of surface differential rotation, which is compatible with a nonsolar type dynamo.

References

- Aigrain, S., Parviainen, H., & Pope, B. J. S. 2016, *MNRAS*, 459, 2408
- Andersen, J. M., & Korhonen, H. 2015, *MNRAS*, 448, 3053
- Anglada-Escudé, G., Amado, P. J., Barnes, J., et al. 2016, *Nature*, 536, 437
- Astudillo-Defru, N., Delfosse, X., Bonfils, X., et al. 2017, *A&A*, 600, A13
- Baliunas, S. L., Donahue, R. A., Soon, W. H., et al. 1995, *ApJ*, 438, 269
- Böhm-Vitense, E. 2007, *ApJ*, 657, 486
- Boisse, I., Bonfils, X., & Santos, N. C. 2012, *A&A*, 545, A109
- Bonfils, X., Delfosse, X., Udry, S., et al. 2013, *A&A*, 549, A109
- Bonomo, A. S., & Lanza, A. F. 2012, *A&A*, 547, A37
- Borucki, W. J., Koch, D., Basri, G., et al. 2010, *Science*, 327, 977
- Brandenburg, A., Saar, S. H., & Turpin, C. R. 1998, *ApJ*, 498, L51
- Buccino, A. P., Lemarchand, G. A., & Mauas, P. J. D. 2007, *Icarus*, 192, 582
- Buccino, A. P., Díaz, R. F., Luoni, M. L., Abrevaya, X. C., & Mauas, P. J. D. 2011, *AJ*, 141, 34
- Buccino, A. P., Petrucci, R., Jofré, E., & Mauas, P. J. D. 2014, *ApJ*, 781, L9
- Buccino, A. P., Sraibman, L., Olivar, P. M., & Minotti, F. O. 2020, *MNRAS*, 497, 3968
- Chabrier, G., & Baraffe, I. 1997, *A&A*, 327, 1039
- Chabrier, G., & Küker, M. 2006, *A&A*, 446, 1027
- Charbonneau, P. 2010, *Living Rev. Sol. Phys.*, 7, 3
- Charbonneau, P., & MacGregor, K. B. 1997, *ApJ*, 486, 502
- Cincunegui, C., & Mauas, P. J. D. 2004, *A&A*, 414, 699
- Cincunegui, C., Díaz, R. F., & Mauas, P. J. D. 2007a, *A&A*, 461, 1107
- Cincunegui, C., Díaz, R. F., & Mauas, P. J. D. 2007b, *A&A*, 469, 309
- Claret, A., & Bloemen, S. 2011, *A&A*, 529, A75
- Cole, E., Brandenburg, A., Kápylä, P. J., & Kápylä, M. J. 2016, *A&A*, 593, A134
- Davenport, J. R. A., Kipping, D. M., Sasselov, D., Matthews, J. M., & Cameron, C. 2016, *ApJ*, 829, L31
- Desort, M., Lagrange, A. M., Galland, F., Udry, S., & Mayor, M. 2007, *A&A*, 473, 983
- Díaz, R. F., Cincunegui, C., & Mauas, P. J. D. 2007a, *MNRAS*, 378, 1007
- Díaz, R. F., González, J. F., Cincunegui, C., & Mauas, P. J. D. 2007b, *A&A*, 474, 345
- Díaz, R. F., Ségransan, D., Udry, S., et al. 2016, *A&A*, 585, A134
- Díaz, R. F., Delfosse, X., Hobson, M. J., et al. 2019, *A&A*, 625, A17
- Díez Alonso, E., Caballero, J. A., Montes, D., et al. 2019, *A&A*, 621, A126
- Dikpati, M., Gilman, P. A., & MacGregor, K. B. 2005, *ApJ*, 631, 647
- Dressing, C. D., & Charbonneau, D. 2015, *ApJ*, 807, 45
- Duncan, D. K., Vaughan, A. H., Wilson, O. C., et al. 1991, *ApJS*, 76, 383
- Durney, B. R., De Young, D. S., & Roxburgh, I. W. 1993, *Sol. Phys.*, 145, 207
- Engle, S. G., & Guinan, E. F. 2011, *ASP Conf. Ser.*, 451, 285
- Engle, S. G., & Guinan, E. F. 2018, *Res. Notes Am. Astron. Soc.*, 2, 34
- Falchi, A., Tozzi, G. P., Falciani, F., & Smaldone, L. A. 1990, *Astrophys. Lett. Commun.*, 28, 15
- Fontenla, J. M., Linsky, J. L., Witbrod, J., et al. 2016, *ApJ*, 830, 154
- Gagné, J., Mamajek, E. E., Malo, L., et al. 2018, *ApJ*, 856, 23
- Gaidos, E., Mann, A. W., Lépine, S., et al. 2014, *MNRAS*, 443, 2561
- García, R. A., Ceillier, T., Salabert, D., et al. 2014, *A&A*, 572, A34
- Giampapa, M. S., & Liebert, J. 1986, *ApJ*, 305, 784
- Gizis, J. E., Paudel, R. R., Mullan, D., et al. 2017, *ApJ*, 845, 33
- Gomes da Silva, J., Santos, N. C., Bonfils, X., et al. 2012, *A&A*, 541, A9
- Günther, M. N., Zhan, Z., Seager, S., et al. 2020, *AJ*, 159, 60
- Hawley, S. L., Gizis, J. E., & Reid, I. N. 1996, *AJ*, 112, 2799
- Hawley, S. L., Davenport, J. R. A., Kowalski, A. F., et al. 2014, *ApJ*, 797, 121
- Haywood, R. D., Collier Cameron, A., Queloz, D., et al. 2014, *MNRAS*, 443, 2517
- Ibañez Bustos, R. V., Buccino, A. P., Flores, M., et al. 2019a, *MNRAS*, 483, 1159
- Ibañez Bustos, R. V., Buccino, A. P., Flores, M., & Mauas, P. J. D. 2019b, *A&A*, 628, L1
- Jenkins, J. S., Jones, H. R. A., Pavlenko, Y., et al. 2008, *A&A*, 485, 571
- Johns-Krull, C. M., & Valenti, J. A. 1996, *ApJ*, 459, L95
- Kiraga, M., & Stepien, K. 2007, *Acta Astron.*, 57, 149
- Lamm, M. H., Bailer-Jones, C. A. L., Mundt, R., Herbst, W., & Scholz, A. 2004, *A&A*, 417, 557
- Lanza, A. F. 2016, *Imaging Surface Spots from Space-Borne Photometry*, eds J.-P. Rozelot, & C. Neiner, 914, 43
- Lanza, A. F., Catalano, S., Cutispoto, G., Pagano, I., & Rodono, M. 1998, *A&A*, 332, 541
- Lanza, A. F., Bonomo, A. S., & Rodonò, M. 2007, *A&A*, 464, 741
- Liu, Y., San Liang, X., & Weisberg, R. H. 2007, *J. At. Ocean. Technol.*, 24, 2093
- Lovis, C., Dumusque, X., Santos, N. C., et al. 2011, ArXiv e-prints [arXiv:1107.5325]
- Malo, L., Artigau, É., Doyon, R., et al. 2014, *ApJ*, 788, 81
- Mauas, P. J. D., & Falchi, A. 1994, *A&A*, 281, 129
- Mauas, P. J. D., & Falchi, A. 1996, *A&A*, 310, 245
- Mauas, P. J. D., Falchi, A., Pasquini, L., & Pallavicini, R. 1997, *A&A*, 326, 249
- McQuillan, A., Aigrain, S., & Mazeh, T. 2013, *MNRAS*, 432, 1203
- Metcalfe, T. S., Buccino, A. P., Brown, B. P., et al. 2013, *ApJ*, 763, L26
- Morris, B. M., Bobra, M. G., Agol, E., Lee, Y. J., & Hawley, S. L. 2020, *MNRAS*, 493, 5489
- Mortier, A., Faria, J. P., Correia, C. M., Santerne, A., & Santos, N. C. 2015, *A&A*, 573, A101
- Muirhead, P. S., Johnson, J. A., Apps, K., et al. 2012, *ApJ*, 747, 144
- Newton, E. R., Irwin, J., Charbonneau, D., et al. 2017, *ApJ*, 834, 85
- Radick, R. R., Lockwood, G. W., Henry, G. W., Hall, J. C., & Pevtsov, A. A. 2018, *ApJ*, 855, 75
- Reiners, A., Joshi, N., & Goldman, B. 2012, *AJ*, 143, 93
- Reiners, A., Zechmeister, M., Caballero, J. A., et al. 2018, *A&A*, 612, A49
- Ribas, I., Tuomi, M., Reiners, A., et al. 2018, *Nature*, 563, 365
- Roberts, D. H., Lehar, J., & Dreher, J. W. 1987, *AJ*, 93, 968
- Robertson, P., & Mahadevan, S. 2014, *ApJ*, 793, L24
- Robertson, P., Mahadevan, S., Endl, M., & Roy, A. 2014, *Science*, 345, 440
- Rodríguez Martínez, R., Lopez, L. A., Shappee, B. J., et al. 2020, *ApJ*, 892, 144
- Saar, S. H., & Brandenburg, A. 1999, *ApJ*, 524, 295
- Suárez Mascareño, A., Reboló, R., & González Hernández, J. I. 2016, *A&A*, 595, A12
- Toledo-Padrón, B., González Hernández, J. I., Rodríguez-López, C., et al. 2019, *MNRAS*, 488, 5145
- Torrence, C., & Compo, G. P. 1998, *Bull. Am. Meteorol. Soc.*, 79, 61
- Tsikoudi, V., & Kellett, B. J. 1997, *MNRAS*, 285, 759
- Vida, K., & Roettenbacher, R. M. 2018, *A&A*, 616, A163
- Vida, K., Kóvári, Z., Pál, A., Oláh, K., & Kriskovics, L. 2017, *ApJ*, 841, 124
- Walkowicz, L. M., & Hawley, S. L. 2009, *AJ*, 137, 3297
- Wargelin, B. J., Kashyap, V. L., Drake, J. J., García-Alvarez, D., & Ratzlaff, P. W. 2008, *ApJ*, 676, 610
- Wargelin, B. J., Saar, S. H., Pojmański, G., Drake, J. J., & Kashyap, V. L. 2017, *MNRAS*, 464, 3281
- West, A. A., Hawley, S. L., Walkowicz, L. M., et al. 2004, *AJ*, 128, 426
- West, A. A., Morgan, D. P., Bochanski, J. J., et al. 2011, *AJ*, 141, 97
- Winters, J. G., Medina, A. A., Irwin, J. M., et al. 2019, *AJ*, 158, 152
- Wright, N. J., & Drake, J. J. 2016, *Nature*, 535, 526
- Wright, N. J., Drake, J. J., Mamajek, E. E., & Henry, G. W. 2011, *ApJ*, 743, 48
- Wright, N. J., Newton, E. R., Williams, P. K. G., Drake, J. J., & Yadav, R. K. 2018, *MNRAS*, 479, 2351
- Yadav, R. K., Christensen, U. R., Wolk, S. J., & Poppenhaeger, K. 2016, *ApJ*, 833, L28
- Zechmeister, M., & Kürster, M. 2009, *A&A*, 496, 577

Appendix A: Additional table

Table A.1. Log of the observations.

Spectrograph	xJD	$\langle S \rangle$	Exp. time (s)	H $_{\alpha}$ /Na I	ID (only REOSC)	Program ID
	3545.000000	6.789795e+00	8400	y/y	0605c	
	3926.000000	9.304848e+00	5400	y/y	0706a	
	3955.000000	7.451568e+00	7200	y/y	0806a	
	4165.000000	7.487149e+00	5400	y/y	0307c	
	4281.000000	4.319932e+00	7200	y/n	0607a	
	4367.000000	5.787213e+00	10 800	y/y	0907a	
	4730.000000	1.124911e+01	10 800	n/n **	0908b	
	4988.000000	1.235089e+01	10 800	y/y	0609a	
	5106.000000	1.087805e+01	10 800	y/y	1009a	
REOSC	5263.000000	1.083528e+01	7200	y/y	0310c	
	5358.000000	8.470264e+00	10 800	y/y	0610c	
	5731.000000	6.674119e+00	10 800	y/n	0611b	
	5819.000000	9.433980e+00	7200	y/y	0911a	
	6089.000000	1.308467e+01	5400	y/y	0612c	
	6172.000000	1.174740e+01	7200	y/y	0912b	
	6434.000000	1.468871e+01	5400	n/n **	0513a	
	6833.000000	8.659113e+00	5400	y/n	0614b	
	8273.000000	1.114678e+01	7200	y/y	0618a	
	8653.000000	9.978682e+00	6000	y/y	0619d	
	3574.136719	6.789795e+00	900	y/y		
	3607.078125	7.501529e+00	900	y/y		072.C-0488(E)
	7492.320312	7.002447e+00	900	y/y		
	7492.328125	6.360152e+00	900	y/y		
HARPS	7493.335938	7.536248e+00	900	n/y		
	7590.027344	6.963389e+00	900	y/y		
	7590.039062	6.768096e+00	900	y/y		
	7593.023438	7.353976e+00	900	y/y		
	7593.035156	7.058867e+00	900	y/y		
	7595.117188	8.495354e+00	1200	y/y		
	7598.207031	7.544929e+00	900	y/y		
	7599.027344	8.256663e+00	900	y/y		
	7599.035156	8.816503e+00	900	y/y		
	7600.050781	7.679464e+00	900	y/y		
	7600.062500	6.828854e+00	900	y/y		
	7603.136719	7.115284e+00	900	y/y		097.C-0864(B)
	7603.148438	6.286373e+00	900	y/y		
	7666.992188	8.365159e+00	900	y/y		
	7667.003906	8.243643e+00	900	y/y		
	7667.980469	6.312413e+00	900	y/y		
	7667.992188	7.991933e+00	900	y/y		
	7671.023438	6.624882e+00	900	y/y		
	7904.171875	6.255995e+00	900	y/y		
	7904.183594	6.442607e+00	900	y/y		
	7905.171875	5.422745e+00	900	y/y		
	7905.183594	5.613698e+00	900	y/y		
	7907.125000	8.217604e+00	900	y/y		
	7907.136719	7.831357e+00	900	y/y		
	7918.199219	8.473655e+00	900	y/y		
	7934.160156	7.006788e+00	900	y/y		
	7936.128906	7.427752e+00	900	y/y		
	7937.148438	7.536248e+00	900	y/y		
	7942.093750	6.381851e+00	900	y/y		
	7943.082031	5.544260e+00	900	n/y		

Notes. Column 1: spectrograph name; Col. 2: xJD = JD – 2 450 000, where JD is the Julian date; Col. 3: mean Mount Wilson S -index; Col. 4: exposure time in seconds; Col. 5: spectrum used in the analysis of Sect. 4 (“y”) or not (“n”), those with a double asterisk were not used in the study because they include flares; Col. 6: CASLEO label corresponding to the date of each observing run (MMYY); Col. 7: ID programs of the Gl 729 public observations.

Table A.1. continued.

Spectrograph	xJD	$\langle S \rangle$	Exp. time (s)	H α /Na I	ID (only REOSC)	Program ID
	7944.066406	8.000612e+00	900	y/y		
	7945.109375	6.442607e+00	900	y/y		
	7946.238281	7.323596e+00	900	y/y		
	7953.214844	7.492851e+00	900	y/y		
	7954.136719	1.232309e+01	900	y/y		
	7961.140625	6.117120e+00	900	y/y		
	7962.132812	8.425916e+00	900	y/y		
	7964.144531	6.946029e+00	900	y/y		
	7972.152344	6.316752e+00	900	y/y		099.C-0880(A)
	7974.152344	6.490346e+00	900	y/y		
	7979.214844	8.126467e+00	900	y/y		
	7985.027344	7.753242e+00	900	y/y		
	7986.039062	7.384354e+00	900	y/y		
	7987.050781	6.603183e+00	900	y/y		
	7990.011719	7.761920e+00	900	y/y		
	7992.027344	5.778612e+00	900	y/y		
	7993.011719	6.229956e+00	900	y/y		
	7994.000000	7.310576e+00	900	y/y		
	7995.003906	9.580315e+00	900	y/n		
	7996.007812	1.016185e+01	900	y/y		
	7998.039062	6.108440e+00	900	y/y		
	8001.042969	7.184721e+00	900	y/y		
	8002.031250	7.084904e+00	900	y/y		
	8018.035156	6.190897e+00	900	y/y		
	8019.003906	6.104101e+00	900	y/y		
	8024.089844	6.099760e+00	900	y/y		
FEROS	4166.343750	7.695313e+00	454	n/n		078.A-9058(A)
	5716.335938	6.269531e+00	230	y/n		
UVES	5716.335938	6.269531e+00	230	y/n		087.D-0069(A)
	5716.339844	6.480469e+00	230	y/n		
	7220.070312	5.832031e+00	500	y/n		095.D-0685(A)
X-shooter	7185.191406	4.931776e+00	120	y/y		095.D-0949(A)
	7185.195312	4.783937e+00	120	n/n		
	1050.335938	4.758584e+00	400	n/n		U05H
	1051.359375	4.904892e+00	600	n/n		
	1312.566406	4.888838e+00	450	n/n		N22H
	1367.378906	4.686143e+00	400	n/n		N20H
	1703.480469	4.811812e+00	500	n/n		N31H
HIRES	2390.609375	7.101417e+00	480	n/n		N11H
	2803.515625	4.032948e+00	480	n/n		U16H
	2834.394531	4.627389e+00	600	n/n		N15H
	3153.507812	4.281481e+00	480	n/n		U10H
	3239.343750	5.095374e+00	500	n/n		U09H
	3548.460938	6.789794e+00	500	n/n		N59H
	3934.335938	6.148695e+00	500	n/n		N054Hr
	5409.390625	6.813473e+00	600	n/n		H222Hr